Combining ADMIRE and MV to Improve Image Quality

Siegfried Schlunk, *Student Member, IEEE*, and Brett Byram, *Member, IEEE*

Abstract— Aperture domain model image reconstruction (ADMIRE) is a frequency-domain, model-based beamformer, in part designed for removing reverberation and off-axis clutter. Minimum variance (MV) is alternatively designed to reduce off-axis interference and improve lateral resolution. MV is known to be less effective in high incoherent noise scenarios, and its performance in the presence of reverberation has not been evaluated. By implementing ADMIRE before MV, the benefits of both these beamformers can be achieved. In this article, the assumptions of MV are discussed, specifically their relationship to reverberation clutter. The use of ADMIRE as a preprocessing step to suppress noise from simulations with linear scanning and *in vivo* curvilinear kidney data is demonstrated, and both narrowband and broadband implementations of MV are applied. With optimal parameters, ADMIRE + MV demonstrated sizing improvements over MV alone by an average of 52.1% in 0-dB signal-to-clutter ratio reverberation cyst simulations and 14.5% *in vivo* while improving the contrast ratio compared to ADMIRE alone by an average of 15.1% in simulations and 14.0% *in vivo*. ADMIRE + MV demonstrated a consistent improvement compared to DAS, MV, and ADMIRE both in terms of sizing and contrast ratio.

Index Terms— Beamforming, image quality, *in vivo*, medical ultrasound, minimum variance (MV), model, reverberation clutter, signal processing, simulation.

I. Introduction

MANY beamformers are designed with specific quality metrics in mind, such as improving contrast ratio or signal-to-noise ratio (SNR). Aperture domain model image reconstruction (ADMIRE) [1]–[3] falls into this camp, with its use primarily intended for decluttering (reducing reverberation clutter, off-axis interference, and other sources of image degradation), which results in generally improved contrast ratio and SNR. Other beamformers may seek to improve resolution, a well-known example of which is minimum variance

(MV). MV is often an attractive beamformer, in part due to its rigorous mathematical basis, dating all the way back to Capon's original implementation in 1969 for use with seismic data [4]. Though the applications of the original version were somewhat limited given the assumptions that are made, it has been adapted for use with ultrasound by many different groups [5]–[15], each looking to address various shortcomings of the original method. However, it is well known that MV still struggles in environments where the signal-to-noise ratio (SNR) is low, and this is especially true in the case of reverberation clutter, as we will demonstrate in Section II.

We have previously shown in simple plane wave simulations with minimal reverberation that ADMIRE can be used prior to applying MV [16]. ADMIRE preserves the dimensionality of the channel data, which means that it can function as a preprocessing step, compared to most other beamformers that are strictly for postprocessing. Since ADMIRE can improve SNR and remove troublesome sources of interference, this opens up the possibility that, by processing with both ADMIRE and MV, we can achieve a combined result that has both improved contrast ratio and lateral resolution. In this article, we expand on our previous work [16], [17] by examining the assumptions of MV to shed some light on the issues, particularly in high reverberation clutter environments and implementing both a narrowband (NB) version and a broadband (BB) version of MV. We also include an expanded set of simulations with different sources of noise and more *in vivo* cases. We demonstrate that ADMIRE + MV can often produce a better contrast ratio and better lateral resolution than ADMIRE or MV alone.

II. Background

A. Applying MV to Ultrasound Imaging

MV is mathematically designed to distinguish between a finite number of sources located in the far-field (fewer than the number of array elements). For a chosen source, when the SNR is high, the beamformer places nulls at the locations of other interfering plane waves (referred to as off-axis), minimizing their contribution and suppressing the interference [4], [18]. Though Capon's MV was formulated with passive sensing of seismic data in mind, conceptually, the process is similar to ultrasound with proper beamforming. Echoes in ultrasound are caused by relatively near-field scatterers compared to seismic signals, and so they appear as curved wavefronts at the transducer. However, by applying correct receive delays to the

echoes near the transmit focus, the received echoes from these scatterers will take on the appearance of plane waves. Then, the echoes from these scatterers can be differentiated based on the direction of propagation of the plane waves, as is done in the original work. In the ultrasound context, these off-axis plane waves are caused by scatterers at a similar depth to the focus but not directly at the focus.

MV has proven itself a useful method for improving lateral resolution though adaptation to ultrasound applications has required addressing some of the limitations and assumptions of the original method. Critics point out that Capon's MV is designed for NB applications in the far-field, with a low correlation between on- and off-axis signals [19]. In addition, the covariance matrix, of which the inversion is required for the calculation, is often insufficiently robust when applied to ultrasound. That being said, these issues have been addressed and rectified by multiple groups.

Sasso and Cohen-Bacrie [5] looked to solve the correlation problem by introducing a spatial smoothing preprocessing step to induce decorrelation, which works by analyzing subarrays and estimating a covariance matrix for each and averaging the set. The NB assumption does not *per se* invalidate the application (and many versions do not make considerations for it), but Holfort *et al.* [7] specifically introduced a BB implementation that breaks down the ultrasound signal in the frequency domain into a set of NB windows, over which the assumption is valid. The far-field assumption can be addressed with proper delaying of the output data, which flattens the incoming echoes. Finally, the lack of robustness of the covariance matrix has been addressed by many authors, and it usually consists of using spatial averaging and diagonal loading to guarantee an invertible matrix. Diagonal loading has been demonstrated by many groups [20]–[22], while spatial averaging was initially used as mentioned for creating decorrelation. Eventually, Synnevåg *et al.* [6] presented a robust version for both diagonal loading and spatial averaging, and discussed optimal parameters for each.

B. Unresolved Problem—Reverberation Clutter

It is known that MV performs worse as noise content increases, but we suggest here that reverberation clutter is particularly problematic. From the original Capon paper [4], it is assumed that incoming signals are unity amplitude monochromatic plane waves. When properly delayed, on- and off-axis signals take the form of plane waves, which mostly satisfies this assumption, but reverberant signals (and other complications, such as phase aberration) do not. Reverberant signals originate from shallower depths than the target and are effectively time-delayed to the target time index by means of multipath scattering. This means that the delays applied to reverberant signals will be mismatched, and those signals will not be flattened into plane waves but, rather, will remain spherical waves. In the case of phase aberration, this problem may be further exaggerated, as there will be no ideal plane waves, and all signals will have spherical components. This is problematic, as we will demonstrate.

In the derivation in Capon's paper [4], he arrives at an important inequality

$$b^2 \gg \frac{R}{K} \frac{|B(\Delta \boldsymbol{k})|^2}{1 - |B(\Delta \boldsymbol{k})|^2}. \quad (1)$$

b is related to the scattering amplitude of the chosen plane wave, R is the ratio of the incoherent noise power to the total power for K sensors, $|B(\Delta \boldsymbol{k})|^2$ is the beamforming array response pattern, and $\Delta \boldsymbol{k}$ is the difference between the vector wavenumber of the chosen and off-axis plane waves. Capon states that the inequality is satisfied when either R/K or $|B(\Delta \boldsymbol{k})|^2$ is small, effectively meaning either when the incoherent noise power is relatively low compared to the number of sensors, or when the difference of the vector wavenumbers $\boldsymbol{k}_1$ and $\boldsymbol{k}_2$ is sufficiently large. In the case of two plane waves that are sufficiently separated (and, thus, have sufficiently different vector wavenumbers) and given a sufficiently low noise level, this method will be able to resolve the two plane waves. Van Trees [18] makes a similar assertion that the SNR must be reasonably high, and at most $K - 2$ interfering plane waves must fall outside of the main lobe for proper nulls to be formed for each of the interfering signals [18].

However, spherical reverberant signals complicate things on multiple levels. It should be noted that, in the Cartesian plane, a given plane wave will have a fixed wavenumber, the direction of which shows the direction of the wave. However, the Weyl expansion tells us that a spherical wave can be written as a linear combination of infinite plane waves [23]–[25]; specifically,

$$\frac{e^{-jk_0 r}}{r} = \frac{1}{j2\pi} \int_{-\infty}^{\infty} \int_{-\infty}^{\infty} e^{-j(k_x x + k_y y)} \frac{e^{-jk_z|z|}}{k_z} dk_x dk_y. \quad (2)$$

A spherical wave with k_0 is then composed of a continuous set of plane waves with vector wavenumbers $\mathbf{k} = [k_x, k_y, k_z]$ that satisfy $k_0 = (k_x^2 + k_y^2 + k_z^2)^{1/2}$. It is then apparent that there will be an overlap between the fixed $\boldsymbol{k}_1$ of our target plane wave and the continuous set of possible values of $\boldsymbol{k}_2$ for the spherical reverberant wave. Therefore, some parts of the reverberant wave will be too similar to $\boldsymbol{k}_1$ and, thus, be unresolvable. In addition, since the goal is to place nulls in the beampattern in the directions of interference (i.e., the plane waves corresponding to sufficiently different vector wavenumbers), this is more difficult in a case where there is a continuous set of plane waves. Thus, the beamformer will struggle with rejecting the continuous set compared to well-defined discrete plane waves. We simulated an example of a point target and a reverberant target in Field II [26], [27], which is included in Fig. 1 to show a visual example of how an on-target plane wave and reverberant spherical wave have vector wavenumbers with inherent overlap. In addition, we see that MV is unable to properly reduce or eliminate the reverberant signal, resulting in somewhat worse resolution of the primary target, though still better than DAS alone. Fig. 1(g) shows an example of the MV beampattern when an off-axis target is present and the resulting null in the beampattern that is formed to suppress that off-axis interference. In comparison, the case where the off-axis target is replaced by a reverberant signal in the same
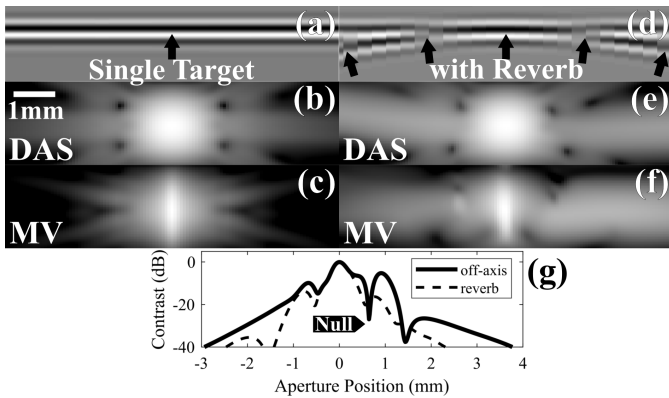
Fig. 1. Field II simulations of an individual point target (a)–(c) without interference and (d)–(f) with reverberant signal interference. The reverberant signal is simulated at a much shallower depth than the point target and then time-delayed to appear at the same time index. (a) and (d) Channel data at the depth of the point target. The arrows indicate the directions of the vector wavenumbers of the echoes, showing a subset of the possible wavenumbers in the reverberant spherical wave case. (b) and (e) DAS and (c) and (f) MV images of the point target. B-mode images are displayed on a 60-dB scale. (g) High-resolution beam plot from MV of a separate simulation where the reverberant signal is replaced with an off-axis target, highlighting the null that is created in the off-axis case and the lack thereof in the reverberation case.

location shows how the beampattern tries to generally suppress the reverberant region, but, from the b-mode images, we see that it is less successful at suppressing that interference.

A final consideration is the ratio of the incoherent noise power, R/K. It is stated that, as long as the noise contribution is relatively low, the two waves could still be distinguishable. Diffuse reverberation clutter takes on a speckle-like appearance in the final image and is relatively incoherent in the aperture domain [28], [29]. Then, in the case of very strong diffuse reverberation clutter, it may have the effect of being strong enough to interfere with the MV beamformer. Supporting this theory, Austeng *et al.* [30] showed that, in the case of very strong phase aberration, MV has comparable performance to DAS with Hamming apodization and slightly worse than DAS with rectangular apodization. Here, we adopt the understanding that diffuse reverberation clutter originates from the complex tissue in the body wall [28], [31], [32].

Overall, reverberant signals and other nonplane wave signals pose an additional challenge for MV due to the inability to fully reject the overlap between the continuous vector wavenumbers present in spherical signals and the discrete vector wavenumber of an on-axis target. In these cases, or, in general, in the presence of strong noise content, MV will struggle or fail to narrow the main lobe, reducing performance.

C. Proposed Solution—Preprocessing With ADMIRE

The primary goal of this work is to improve the performance of MV in these high reverberation clutter or complex *in vivo* environments. To that end, we propose that a preprocessing step before MV to remove these sources of interference will do exactly that. ADMIRE is a method for removing reverberation and off-axis clutter, as well as suppressing wavefront aberration [1]–[3]. Crucially, for this work, ADMIRE is

a somewhat unique beamformer in that, when it processes channel data, it does not alter the dimensionality of the input data. This means that we can subsequently process the decluttered data with other beamforming methods, in this case, MV. We hypothesize that ADMIRE will be able to suppress these difficult sources of interference, removing the spherical components that MV struggles with and generally reducing the number of interfering waves and improving effective SNR, making it possible for MV to perform better than without preprocessing. This gives us the possibility to create better images than with either method alone.

III. BEAMFORMING ALGORITHMS

We implemented all beamformers in MATLAB (The Math-Works, Natick, MA, USA).

A. Delay-and-Sum (DAS)

The DAS beamformer is defined by

$$S_{\text{DAS}}(x, z) = \sum_{i=1}^{M} w_i(x, z) s_i(x, z) \quad (3)$$

where S is the resulting image prior to enveloping or log compression, x is the index for the a-line of the final image, z is a discrete-time index, M is the total number of channels, $w_i(x, z)$ is the weighting factor for channel i, and $s_i(x, z)$ is the delayed channel data. The weighting factor accounts for receive apodization and can vary by depth and channel (taking F-number into consideration) or be static as in the case of a fixed rectangular window, where all channels are weighted equally. Adjusting this weighting using Hamming apodization has been shown to reduce sidelobes [33]. In this work, we will use both normal DAS with fixed rectangular apodization to show the raw data (DAS) and also DAS with Hamming apodization as a commonly used weighting scheme (DAS-Hamm).

B. Minimum Variance

MV can be thought of as an adaptively weighted and delayed DAS image where the weighting factor is optimized to improve lateral resolution by reducing off-axis clutter [6], [7]. Bold characters here and for the rest of the text indicate vectors. The optimized weights are defined as

$$\mathbf{w} = \frac{R^{-1}\mathbf{e}}{\mathbf{e}^H R^{-1}\mathbf{e}} \quad (4)$$

where $\mathbf{e}$ is the steering vector, H is the conjugate transpose, and R is the covariance matrix defined as

$$R(x, z) = E[\mathbf{s}(x, z)\mathbf{s}(x, z)^H] \quad (5)$$

where $E[\cdot]$ denotes the expectation and $\mathbf{s}(x, z)$ is the delayed aperture signal at lateral index x and depth z. To ensure that R is invertible, we used subarray averaging and diagonal loading methods [6]. The recommendations provided are to use subarray lengths of $L = 0.5\,M$ and diagonal loading defined

as $\epsilon = \Delta \cdot \mathrm{tr}(\hat{R})$, where $\Delta = 1/(10L)$ [6]. The estimated MV signal is then defined as

$$\hat{S}_{\mathrm{MV}}(x, z) = \frac{1}{M - L + 1} \sum_{l=0}^{M-L} \mathbf{w}(x, z)^H \bar{\mathbf{s}}_l(x, z) \qquad (6)$$

where $\bar{\mathbf{s}}(x, z)$ is the delayed channel data for a given subarray. We will call this version of MV the NB version, abbreviated as MVNB, but we additionally implemented the BB version devised by Holfort *et al.* [7], which we will denote as MVBB. For both implementations, the optimal parameters for subarray averaging and diagonal loading were estimated based on both simulated and *in vivo* data. While diagonal loading does have a small impact on image metrics, it is dwarfed by the impact of subarray averaging, so, for consistency, we use $\Delta = 1/(10L)$, unless stated otherwise. We include, in the results, multiple subarray averaging cases to demonstrate the effect that it has on resolution and sizing.

C. Aperture Domain Model Image Reconstruction

ADMIRE is a method for removing reverberation and off-axis clutter, as well as suppressing wavefront aberration. Byram *et al.* [1] presented a detailed explanation of the components of the algorithm, and additional specifics can be found elsewhere [2], [3].

Processing occurs primarily in the frequency domain. Dynamically delayed channel data are subdivided into multiple overlapping windows by depth, along which the Fourier transform is performed [i.e., a short-time Fourier transform (STFT)]. This produces a set of primary frequency components, each of which is analyzed with a physics-based model. This model contains the predicted aperture domain signal responses for scatterers from all throughout the imaging space. These predicted signals can be calculated based on the well-defined physics of linear wave propagation, similar to other linear simulation tools. These signals are defined by the following equation:

$$p_s(x; t, \omega) = \sum_{n=0}^{N-1} A(x; x_n, z_n, \tau_n, \omega) e^{jk\tau(x; x_n, z_n, \tau_n)} \qquad (7)$$

where x is the position along the aperture, t and ω specify the time and frequency for the signal, k is the corresponding wavenumber, N is the total number of scatterers arriving at the transducer at time t, and $\tau(x; x_n, z_n, \tau_n)$ is the wavefront delay for a signal received from (x_n, z_n) at time τ_n. Note that τ_n can be different from t so that subtle shifts in phase can be included in the model. Finally, $A(x; x_n, z_n, \tau_n, \omega)$ is the amplitude modulation across the aperture caused by the STFT windows and element sensitivity.

The true value for N, the number of scatterers that make up an observed signal, is unknowable. However, by oversampling the imaging space, we can combine all of the individually modeled signals into a model matrix, X, which gives the model the flexibility to represent even a complex observed aperture domain signal, y, by its component sources as
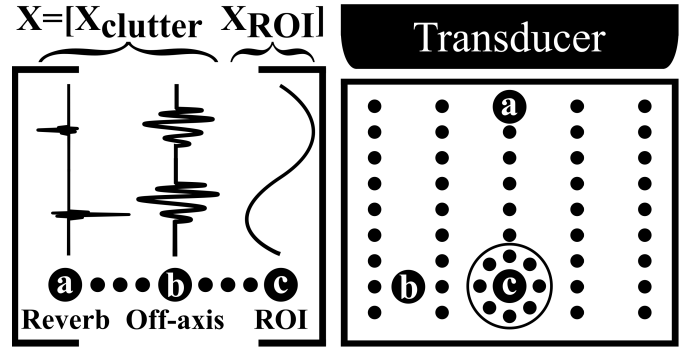
$$y = X\beta \qquad (8)$$

Fig. 2. Example of an ADMIRE model X, composed of a set of estimated signals from locations considered to be clutter [sparsely sampled, e.g., (a) and (b)] and a set from locations considered to be ROI [highly sampled, e.g., (c)]. For a given aperture domain signal y, the model can be used to estimate which sources are components of the received signal, allowing us to remove signal components that are not from the ROI.

where y is the post-STFT signal corresponding to a specific frequency and a given a-line x_n and depth z_n, X is the set of physical model predictors, and β is the unknown set of model coefficients that we solve for. Fig. 2 is included to give an intuitive sense of how each signal in the model matrix X relates to a specific physical source location and, in particular, shows how the model is composed of clutter signals (X_{clutter}, those signals that we consider noise or clutter) and region of interest (ROI) signals (X_{ROI}, signals that we want to keep). Solving (8) reveals the composition of β, each entry of which corresponds to one of those physical locations in the imaging space. This gives us a breakdown of what physical locations are contributing to the aperture domain signal since they linearly combine to form y. By zeroing those coefficients corresponding to signals outside of the ROI, we can simply reconstruct the decluttered aperture signal with

$$y_{\mathrm{decluttered}} = X\beta_{\mathrm{ROI}}. \qquad (9)$$

Defining the ROI as some small region around (x_n, z_n) removes any signals located off-axis or from reverberant sources.

In practice, (8) is ill-posed due to the relatively small size of y compared to the potentially large size of X depending on the sampling of the model space. To solve for the model predictors, ADMIRE uses the elastic-net regularization technique [34] with the optimization equation

$$\hat{\beta} = \arg\min_{\beta}(||y - X\beta||^2 + \lambda(\alpha||\beta||_1 + (1 - \alpha)||\beta||_2^2/2)) \qquad (10)$$

where $||\beta||_1$ is the L1 norm, $||\beta||_2$ is the L2 norm, and α is a user-defined parameter set between 0 and 1 to control the weighting between L1 and L2. λ is a regularization parameter that controls the degrees of freedom [35]. The general recommendation is to choose $\alpha = 0.9$ and $\lambda = (0.0189/10)y_{\mathrm{rms}}$ based on the root mean square (rms) of the signal y. These parameters are chosen based on previous work [1], [2] and are generally robust across most imaging scenarios.

Once the aperture domain signal has been decluttered using the coefficients solved by the elastic net and (9), the inverse

STFT is applied to return to the time domain [36]. This results in a decluttered version of the channel data. As with MV, we tested multiple possible values for our α and λ parameters but found that the default options listed produced the best resolution both in simulations and *in vivo*.

In summary, since ADMIRE can distinguish between echoes that return from different locations in the image, as represented in Fig. 2, this allows the algorithm to selectively keep only those signals that return from the ROI. Signals that originate from close to the transducer, such as reverberant signals, appear fundamentally different from those signals in the ROI, allowing the elastic net to differentiate between the two during the deconstruction. The same is true for other sources of image degradation, such as off-axis clutter.

D. Post ADMIRE Processing

Since ADMIRE returns decluttered channel data, we can, in theory, apply any beamforming method to data that have already been processed with ADMIRE. Most commonly, we simply sum the decluttered channel data like in DAS beamforming, but, rather than write ADMIRE + DAS, we simply refer to this as ADMIRE. For this work, we consider the additional possibility where we apply MV instead of DAS, producing two cases: ADMIRE + MVNB for NB MV and ADMIRE + MVBB for BB MV, abbreviated as AD + MVNB and AD + MVBB, respectively.

As we did with ADMIRE and MV individually, we tested multiple parameter choices for the combined methods AD + MVNB and AD + MVBB. We found that the default ADMIRE parameters continued to be optimal, and changes to diagonal loading in MV were generally imperceptible, except *in vivo* where we were able to see measurable improvement to AD + MVNB by reducing the diagonal loading to $\Delta = 1/(100L)$. Similar to when applying MV alone, changing the length of the subarrays had a significant impact on the resulting image and metrics, so we included these results and some discussion in the following.

IV. METHODS

A. Simulated Speckle Texture for Measuring SNR

We mentioned that ADMIRE can improve SNR, which would be beneficial to MV. To demonstrate this, we simulated a simple speckle texture in Field II [26], [27] using the simulation parameters in Table I. We then created 30 independent realizations of Johnson–Nyquist (thermal) noise by simulating normally distributed independent random noise using the randn function in MATLAB to effectively create 30 "frames" of independent noise. We combined the thermal noise and speckle channel data such that it satisfied a specified SNR as defined by

$$\text{SNR} = 10\log_{10}\left(\frac{P_{\text{SOI}}}{\alpha^2 P_{\text{thermal}}}\right) \quad (11)$$

where P_{SOI} is the power of the channel data of the speckle phantom, P_{thermal} is the power of the channel data of the thermal noise, and α is the scalar for the thermal noise in order

TABLE I
FIELD II SIMULATION PARAMETERS FOR
CONTRAST TARGET PHANTOMS

Parameter	Value
Number of elements	117
Number of mathematical elements (lateral)	7
Number of mathematical elements (elevation)	11
Element height	4 mm
Element width	0.254 mm
Kerf	0.003 mm
Lateral pitch	0.257 mm
Center frequency (f_c)	3 MHz
Sampling frequency (simulation) (f_s)	640 MHz
Sampling frequency (downsampled) (f_s)	40 MHz
Bandwidth	60%
Transmit focal depth	3 cm
Transmit/receive f-number	1

to achieve the desired SNR. For this simulation, we targeted an SNR of 0 dB.

These simulations were then processed with ADMIRE, and the SNR was calculated before and after ADMIRE. We calculated SNR using two methods. The first way, we used the following equation:

$$\text{SNR}_{\text{power}} = 10\log_{10}\left(\frac{P_{\text{signal}}}{P_{\text{noise}}}\right) \quad (12)$$

where P_{signal} is estimated from the average across all 30 frames and P_{noise} was then estimated from the difference between each frame and the estimated signal. Since the signal is static across all frames, the signal power is calculated from the average of the estimated signal, and the noise power is calculated from the variance of all of the frames. The second method was to use the correlation between frames to estimate SNR, as done by Friemel *et al.* [37]. By calculating the correlation coefficient ρ between each successive frame, the SNR can also be estimated by

$$\text{SNR}_{\text{frame}} = 10\log_{10}\left(\frac{\rho}{1-\rho}\right). \quad (13)$$

B. Simulated Single-Target Phantoms

We simulated a single-point target using Field II to demonstrate how MV behaves when a primary target is receiving interference from a reverberant target. The simulation parameters are given in Table I. The primary target was simulated at a depth of 3 cm, while the reverberation target was simulated at a depth of 0.5 cm and then time-shifted to the same time index as our primary target, similar to how reverberation clutter has been simulated in previous work [38], [39]. We could then observe how the point spread function (PSF) differs for MVNB and MVBB versus AD + MVNB and AD + MVBB without and with that reverberation clutter. We in part used the width of the PSF as an indicator for determining the optimal parameters for both MV methods and post-ADMIRE methods.

C. Simulated Cyst Phantoms

To represent the scenario of high noise power reverberation clutter, we used Field II to simulate 5-mm diameter anechoic

cysts using the same parameters as in Table I, creating six independent speckle realizations. We then simulated diffuse reverberation clutter using the method described by Byram and Shu [38], [39]. We added the reverberation clutter such that it satisfied a 0-dB signal-to-clutter ratio (SCR) compared to the cyst channel data. Though there has been relatively little research into classifying what low or high reverberation clutter levels are in terms of SCR, we have previously determined that 0-dB SCR is a plausible representation of clutter corresponding to a difficult-to-image patient [40]. This is backed up by other studies such as one where bladder wall (signal)-to-clutter ratios calculated from image data were between 30 and 0 dB for all sources of clutter, including reverberation [41], suggesting that our target for channel data is reasonable for *in vivo* scenarios.

To complement the reverberation clutter simulations, we also simulated Johnson–Nyquist (thermal) noise, which was added to the cyst channel data at the same 0-dB ratios. We differentiate these thermal noise cases using the abbreviation SNR.

D. In Vivo Kidney Stone Data

We additionally captured *in vivo* kidney data from patients suffering from kidney stone disease using a Verasonics Vantage Ultrasound System (Verasonics, Inc., Kirkland, WA, USA) with a C5-2 curvilinear transducer. A plane wave synthetic aperture acquisition was employed [42], where plane waves were transmitted at multiple angles to achieve focusing at all depths. A center frequency of 4.1667 MHz was used to acquire 64 angles spanning 37°. The data were acquired under protocols approved by the Vanderbilt University IRB (IRB# 170001).

E. Image Quality Metrics

For the simulated cyst phantoms, we computed the contrast ratio and the generalized contrast-to-noise ratio (gCNR) [43], [44], and as a resolution metric, we included radial cyst edge width [45]. The contrast ratio was defined as

$$\text{contrast ratio} = -20\log_{10}\left(\frac{\mu_{\text{ROI}}}{\mu_{\text{background}}}\right) \qquad (14)$$

where μ is the mean value calculated from the enveloped data, before log compression. gCNR is a generalized detectability metric, which measures the overlap of the probability density function between the ROI and the background, making it more robust against stretches or compressions in dynamic range. We used the conventional 100 bins for the histogram estimation for this method. For these metrics, the ROI was defined as the interior of the cyst, and the background was an equivalently sized radial region surrounding the cyst.

In addition to calculating the width of the PSF in our point target simulation, we estimated radial cyst edge width similar to Bottenus *et al.* [45] as a more practical measure of lateral resolution by radially averaging values of equal distance from the center of the cyst within $\pm10°$ of the lateral axis. This produces a function of intensity versus radius, which is normalized by subtracting by μ_{ROI} and scaling by $\mu_{\text{background}}$.
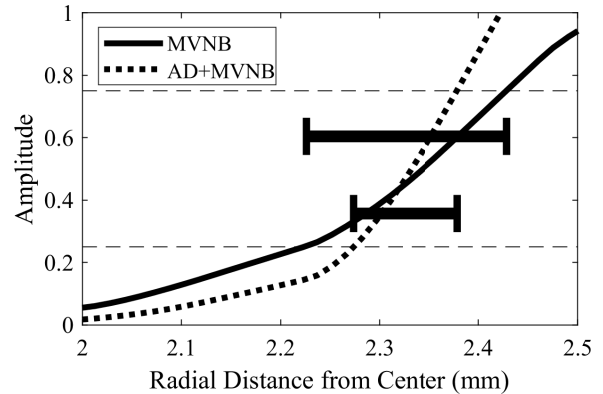

Fig. 3. Example of MVNB and AD + MVNB radial intensity curves from which the cyst edge width is estimated as the distance that it takes to rise from 0.25 to 0.75 (indicated with the dashed lines).

Then, the width is estimated as the rise distance on this curve. This is done for both the left- and right-hand sides of the anechoic cysts. An example showing two such radial intensity curves is shown in Fig. 3. For this work, we considered the rise distance from 0.25 to 0.75, representing a measurement similar to that of the FWHM, as has been done with similar methods in previous work [46].

For the *in vivo* kidney stone cases, the stone ROI was manually selected on a 30-dB dynamic range b-mode image with a contour map as reference. A radial background region was then automatically calculated as 1.5 times the size of the selected stone, centered on the stone. This allowed us to calculate the contrast ratio and gCNR of the stone for all cases and provided a lateral measure of the stone size. Since kidney stones behave as coherent targets [47]–[49], we consider smaller measures of stone size to be an improvement. We also estimate the SNR in these cases by implementing the robust version of the lag-one coherence method devised by Vienneau *et al.* [50] based on original work by Hyun *et al.* [51] and Long *et al.* [52]. Similar to the simulations, this was estimated before and after processing with ADMIRE. In these *in vivo* cases, since we lack the multiple frames required to differentiate thermal noise from other clutter types, the SNR value estimated represents the combination of all types of noise: thermal, reverberation, or others.

To complete our parameter testing for MV and ADMIRE, we tested our suite of parameter choices on both the simulated cysts, and some of the *in vivo* cases to determine if the optimal parameters change between simulations and the *in vivo* data. Examples of interesting parameters are included in the results section to demonstrate how these choices can impact our image quality metrics.

F. Histogram Matching

We include as a supplementary material the histogram matching [53] results and discussion for all the anechoic cyst simulations and *in vivo* cases above to compare against the image quality metrics calculated when no matching is performed. These results are purely supplementary for those

TABLE II
BRIGHT TARGET SIMULATION METRICS

| | PSF Width at Various Amplitudes (mm) | | | |
| | No Reverb | | With Reverb | |
Amplitude	-6 dB	-30 dB	-6 dB	-30 dB
DAS	0.493	0.939	0.503	6.284
MVNB L=0.5M	0.080	0.631	0.174	4.155
MVNB L=0.75M	**0.059**	**0.411**	0.097	0.561
MVBB L=0.5M	0.110	0.863	0.216	5.097
MVBB L=0.75M	0.116	0.939	0.142	0.768
ADMIRE	0.463	0.939	0.471	1.187
AD+MVNB L=0.5M	0.153	0.868	0.084	0.671
AD+MVNB L=0.75M	0.119	0.752	**0.058**	**0.465**
AD+MVBB L=0.5M	0.160	0.895	0.284	1.123
AD+MVBB L=0.75M	0.204	0.939	0.129	0.658

readers interested and will not be discussed in the main text presented here.

V. RESULTS

A. Simulated Speckle SNR Results

From the 30 realizations of independent thermal noise, both SNR_{power} and SNR_{frame} were calculated before and after ADMIRE. SNR_{power} increased from 0.984 to 22.8 dB after ADMIRE. Average SNR_{frame} increased from 0.72 ± 0.01 to 22.65 ± 0.08 dB after ADMIRE. Both methods show that ADMIRE produces a significant increase in SNR.

B. Point Target Simulation Results

The PSFs of the point target simulation results are shown in Fig. 4 to demonstrate the impact of the subarray averaging parameter on MV. To summarize the differences caused by subarray averaging, we focused on two cases, $L = 0.5$ M and $L = 0.75$ M, for both MVNB and MVBB with and without ADMIRE. The PSF for each case is shown in Fig. 4(b) and (d), while the widths of the PSF for each case at -6 and -30 dB are included in Table II. From these results alone, MVNB benefits significantly from increasing the subarray size regardless of reverberation level. In comparison, MVBB prefers $L = 0.5$ M for the no reverberation case and $L = 0.75$ M for the with reverberation case. From the PSF plot in the figure, MVBB behaves rather erratically when the subarray size gets large, whereas MVNB has a more uniform improvement with increased subarray size. As a result, we generally include both parameter choices for MVNB while focusing on $L = 0.5$ M for MVBB in the simulated results.

Fig. 4 also shows that ADMIRE behaves almost identically to DAS, only slightly improving the sidelobes off-axis in the reverberation case. In comparison, MVNB at $L = 0.75$ M has by far the best performance when there is no reverberation clutter (or any significant noise source) present. Even at $L = 0.5$ M, it still outperforms all other beamformers, including the combined method AD + MVNB, though this still performs better than just ADMIRE by itself. However, in the presence of a strong reverberation signal, MVNB suffers substantially with the full-width at half-maximum increasing by 64%. In this case, preprocessing with ADMIRE grants
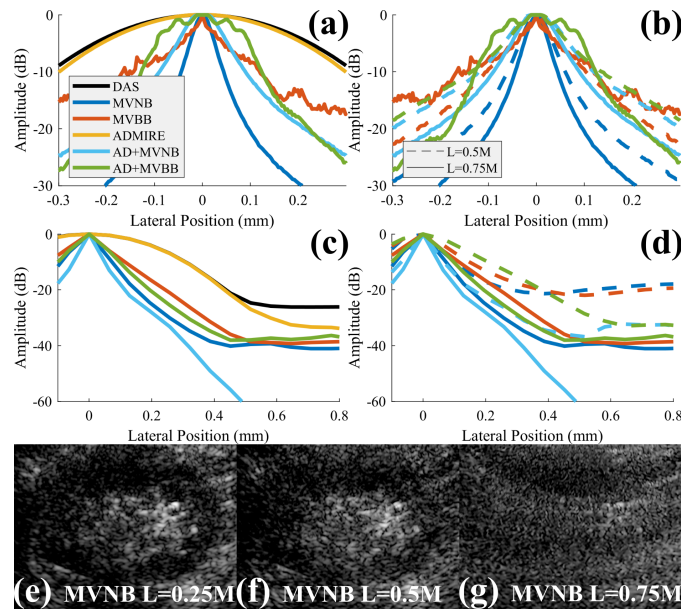

Fig. 4. Parameter testing for the subarray length (L) versus the full aperture length (M) for both NB (MVNB) and BB (MVBB) implementations. PSFs for (a) and (b) bright target with no reverberation interference and (c) and (d) bright target with an interfering reverberant signal. (e)–(g) In vivo example of MVNB with varying subarray lengths, demonstrating how increasing the subarray length can lead to general image quality degradation.

a significant increase in performance, with AD + MVNB performing in the reverberation case equivalently to how MVNB alone performed in the noise-free case. Strangely, AD + MVBB generally performed poorly, worse than running just MVBB alone, regardless of the choice of parameters. However, regardless of NB or BB, the combined method uniformly performed better than just ADMIRE alone and by extension also DAS.

C. Anechoic Cyst Simulation Results

The MVNB cases for the simulated cysts in Fig. 5 show that increasing the subarray size can result in the degradation of the speckle in the background. As expected from this, Table III shows that cyst edge width and contrast ratio are improved with higher subarray sizes though gCNR is lost as a result. This means that the ideal subarray size in these cases may depend on which metrics are more important for a given application. Since both subarray size choices produce viable images, we included both in the tables and figures for MVNB.

The example cysts in Fig. 5 and the cyst edge width measurements in Table III show a general agreement with the bright target simulations. These simulations are split into a noise-free case, a reverberation clutter case (0-dB SCR), and a thermal noise case (0-dB SNR). In these cases, we measured cyst edge width as a complement to PSF width in the bright target simulations and additionally showed more traditional image quality metrics: contrast ratio and gCNR. Unlike in the simple bright targets, in these cases, AD + MVNB ($L = 0.75$ M) always outperforms ADMIRE and MVNB alone in terms of both cyst edge width and
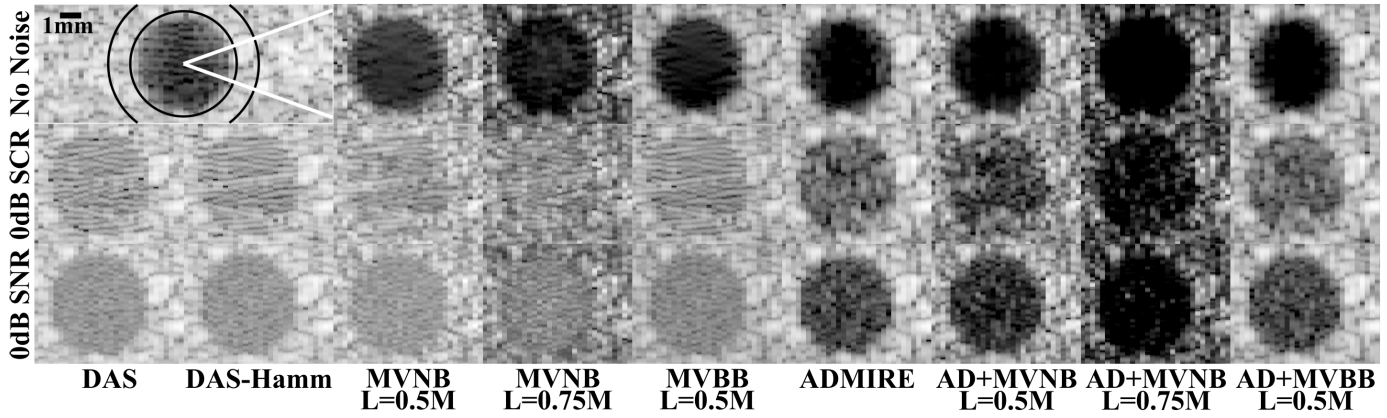
Fig. 5. Sample cases of an anechoic cyst with no added noise, added reverberation clutter (0-dB SCR), and added thermal noise (0-dB SNR) displayed on a 50-dB dynamic range. The black solid circles indicate the true region of the cyst and a background speckle region surrounding it for use with our imaging metrics. The white solid lines show the radial region for which the cyst boundary width was estimated.

TABLE III
ANECHOIC CYST SIMULATION METRICS

| | Cyst Edge Width (mm) | | |
Added Interference	None	0dB SCR	0dB SNR
DAS	0.189±0.025	0.216±0.154	0.171±0.015
DAS-Hamm	0.218±0.028	0.347±0.274	0.202±0.060
MVNB L=0.5M	0.305±0.230	0.641±0.623	0.303±0.291
MVNB L=0.75M	**0.101±0.037**	0.292±0.362	0.155±0.134
MVBB L=0.5M	0.204±0.029	0.437±0.395	0.259±0.282
ADMIRE	0.162±0.022	0.218±0.179	0.138±0.022
AD+MVNB L=0.5M	0.132±0.028	**0.140±0.054**	0.121±0.033
AD+MVNB L=0.75M	**0.098±0.026**	0.183±0.174	**0.105±0.021**
AD+MVBB L=0.5M	0.178±0.017	0.184±0.130	0.154±0.016
	Contrast Ratio (dB)		
Added Interference	None	0dB SCR	0dB SNR
DAS	-31.9±1.1	-12.1±0.7	-14.3±0.7
DAS-Hamm	-38.8±0.8	-11.4±1.1	-14.0±0.7
MVNB L=0.5M	-30.3±1.0	-7.97±1.1	-10.2±0.8
MVNB L=0.75M	-24.4±1.7	-4.83±1.4	-5.58±0.8
MVBB L=0.5M	-36.6±0.7	-10.0±0.9	-12.0±0.7
ADMIRE	-43.1±1.3	-21.5±1.5	-29.9±1.1
AD+MVNB L=0.5M	-42.1±1.4	-21.0±1.7	-30.4±1.4
AD+MVNB L=0.75M	**-46.1±1.5**	**-24.7±2.6**	**-33.5±2.4**
AD+MVBB L=0.5M	**-46.7±1.3**	-20.5±1.7	-29.5±1.2
	generalized Contrast-to-Noise Ratio (gCNR)		
Added Interference	None	0dB SCR	0dB SNR
DAS	0.992±0.003	0.774±0.032	0.932±0.015
DAS-Hamm	**0.999±0.002**	0.745±0.061	0.923±0.016
MVNB L=0.5M	0.969±0.014	0.489±0.055	0.725±0.026
MVNB L=0.75M	0.819±0.028	0.232±0.045	0.390±0.021
MVBB L=0.5M	0.994±0.002	0.649±0.055	0.854±0.020
ADMIRE	0.992±0.005	**0.879±0.030**	**0.982±0.011**
AD+MVNB L=0.5M	0.988±0.005	0.750±0.060	0.930±0.022
AD+MVNB L=0.75M	0.792±0.073	0.676±0.047	0.783±0.095
AD+MVBB L=0.5M	**0.997±0.003**	**0.863±0.046**	**0.983±0.009**

contrast ratio but loses some gCNR compared to ADMIRE to compensate. Even AD + MVNB ($L = 0.5$ M) performs similar to ADMIRE in terms of contrast ratio and gCNR, and still demonstrates an improved cyst edge width compared to both methods. Interestingly, in the high reverberation clutter case (0-dB SCR), AD + MVNB ($L = 0.5$ M) has a better cyst edge width compared to AD + MVNB ($L = 0.75$ M),

suggesting that the loss of gCNR, in that case, did impact the cyst edge appearance. This is also reflected in the much lower variance in the reverberation case for AD + MVNB ($L = 0.5$ M) compared to all other methods, showing consistency similar to the noise-free and thermal noise cases. A final observation is that AD + MVBB never demonstrates any significant improvement compared to just ADMIRE in any of the three cases. Overall, AD + MVNB generally outperforms all of the other methods, with the benefits being most readily apparent in the reverberation clutter and thermal noise cases.

D. In Vivo Kidney Stone Results

Fig. 4(e)–(g) shows different choices of subarray sizes for MVNB for *in vivo* Case 1. Compared to the simulated data, this case shows very obvious image degradation as the subarray size increases, to the point where the image is no longer recognizable as a kidney at $L = 0.75$ M. Since image quality is critical to delineating the kidney stone, $L = 0.25$ M was better for all cases (necessary to identify the kidney stones correctly). The exception to this was AD + MVNB for which increasing subarray averaging to $L = 0.5$ M without losing image quality was possible.

Case 1 with the optimal MV parameters is shown in Fig. 6. Visually, an improvement in general image contrast with ADMIRE-based methods is seen compared to non-ADMIRE-based methods. The general image clarity and boundaries of the kidney also appear the most defined in the AD + MVNB image, and the highlighted kidney stone (marked by the red arrow) appears sharper compared to ADMIRE alone (or any other method). Fig. 7 shows Case 1 and several others zoomed in specifically on the kidney stone of interest, with the stone region drawn in red. The measured stone size is indicated on the images by the blue line and also included along with contrast ratio and gCNR in Table IV. In these *in vivo* cases, both AD + MVNB and AD + MVBB generally perform well, shrinking the apparent size of the stone and boosting contrast ratio and gCNR compared to ADMIRE, MV, or DAS, suggesting better prospects for AD + MVBB compared to the simulations. The only case where the combined methods do not improve upon ADMIRE or MV is Case 5, which is
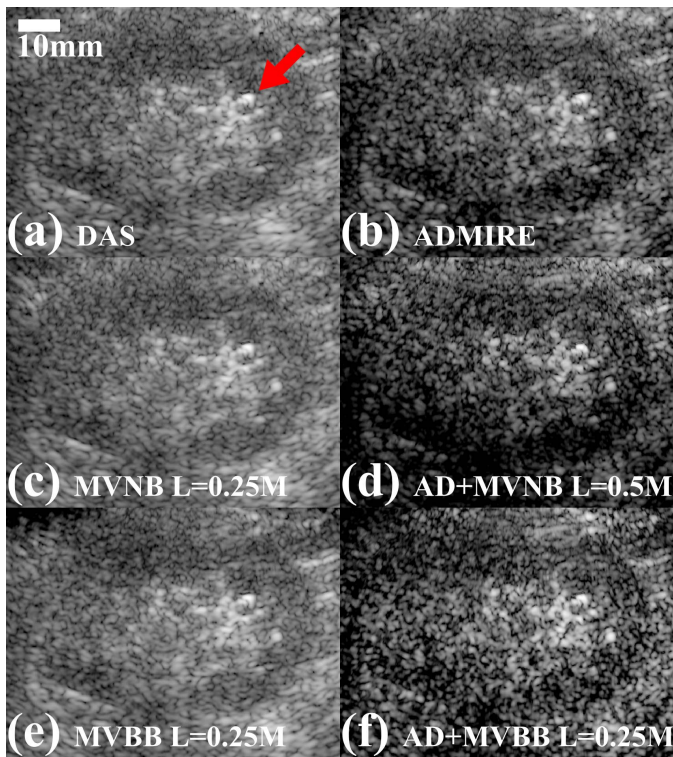
Fig. 6. Comparisons of the b-mode images for Case 1 on a 60-dB dynamic range for the MV methods both individually (c) and (e) and after preprocessing with ADMIRE (d) and (f). The kidney stone is indicated by the red arrow in the DAS image.

TABLE IV
IMAGE METRICS FOR *In Vivo* KIDNEY CASES

Case	Measured Stone Size (mm)					
	1	2	3	4	5	6
DAS	0.489	0.445	0.814	0.482	0.595	0.535
DAS-Hamm	0.526	0.457	0.812	0.486	0.623	0.550
MVNB L=0.25M	0.495	0.473	0.813	0.593	0.595	0.550
MVBB L=0.25M	0.508	0.432	0.791	0.505	0.611	0.555
ADMIRE	0.508	0.407	0.750	0.498	**0.576**	0.495
AD+MVNB L=0.5M	**0.432**	0.367	0.734	0.437	0.623	**0.437**
AD+MVBB L=0.25M	0.501	**0.356**	**0.695**	**0.385**	0.638	0.471
Case	Contrast Ratio (dB)					
	1	2	3	4	5	6
DAS	19.0	14.6	9.68	13.9	11.5	11.4
DAS-Hamm	18.5	16.4	10.0	13.9	12.0	11.5
MVNB L=0.25M	18.3	14.8	9.74	13.6	10.9	11.2
MVBB L=0.25M	18.6	15.8	10.5	13.9	10.9	11.3
ADMIRE	21.6	19.3	8.14	14.9	12.7	14.0
AD+MVNB L=0.5M	**23.6**	**23.3**	9.71	**16.4**	**13.7**	16.6
AD+MVBB L=0.25M	21.8	21.2	**11.6**	15.5	10.6	**17.2**
Case	generalized Contrast-to-Noise Ratio (gCNR)					
	1	2	3	4	5	6
DAS	0.781	0.649	0.582	0.683	0.632	0.609
DAS-Hamm	0.781	0.726	0.609	0.721	0.661	0.600
MVNB L=0.25M	0.800	0.633	0.603	0.680	0.563	0.598
MVBB L=0.25M	0.793	0.716	**0.618**	0.676	0.603	0.593
ADMIRE	0.862	0.748	0.566	0.670	0.642	0.700
AD+MVNB L=0.5M	**0.895**	**0.893**	0.579	**0.749**	**0.707**	**0.798**
AD+MVBB L=0.25M	0.855	0.878	0.615	0.705	0.471	0.785

included in the figure. From the b-mode images, it would seem that the surrounding tissue complicates the case, such that, even with improved resolution, the distinction between stone and background tissue is ambiguous, resulting in no improvement to sizing. The contrast ratio and gCNR are still both improved. The estimated SNR for all noise sources based on the lag-one coherence improved, on average, in these cases from -0.49 ± 5.99 dB before ADMIRE to 20.75 ± 1.32 dB after processing with ADMIRE.

Both the NB and BB implementations of MV perform well *in vivo*, with AD + MVNB averaging slightly better statistics and appearing somewhat better in the b-mode images corresponding to generally better gCNR. However, both methods do succeed at what they were designed to do. The two combined methods each measure the smallest stone size in three of the six cases, with AD + MVNB being slightly more consistent at improving contrast ratio and gCNR compared to ADMIRE or the base MV methods.

VI. DISCUSSION

AD + MVNB demonstrated an improvement over ADMIRE and MVNB in every case, simulated and *in vivo*, with the exception of the noise-free single bright target simulation. AD + MVBB was unimpressive in simulations, performing similar to ADMIRE, but showed similar improvements *in vivo* compared to the NB version. ADMIRE combined with MV overall showed improvements to resolution and general imaging quality metrics, especially in the cases with high

reverberation clutter or thermal noise. Our primary hypothesis in this work was that ADMIRE could remove sources of reverberation and off-axis clutter that would otherwise degrade the performance of MV. Our simulations clearly demonstrate that high noise reduces the ability of MV to properly separate signals and improve resolution though this has been well-known since the original implementations of MV. However, we did show that both versions of MV struggle significantly more when the interference is reverberation clutter compared to thermal noise, even when both are presented at similar signal-to-noise levels. While we can increase the subarray size to compensate for the increased noise presence, this comes at a severe cost of degraded image quality and does not fully mitigate the added noise. We have shown that by preprocessing with ADMIRE, we can improve the resolution and contrast ratio compared to MV alone and outperform ADMIRE in terms of resolution and often in terms of contrast ratio as well.

The NB implementation of MV showed the most universal promise when complemented with ADMIRE, demonstrating noticeable and consistent improvements in the simulations and *in vivo*. AD + MVBB suffered somewhat in simulations, performing generally worse compared to ADMIRE, though still an improvement compared to MVBB alone. This may be due in part to some interactions with the way data are simulated and the similarity of processing that occurs for both ADMIRE and MVBB since both take advantage of the frequency spectrum to process data in an NB fashion in similar ways. Whatever the exact cause, this phenomenon does not carry over to the *in vivo* results, where AD + MVBB generally shows improvements compared to both ADMIRE and MVBB. However, MVNB does slightly outperform MVBB,
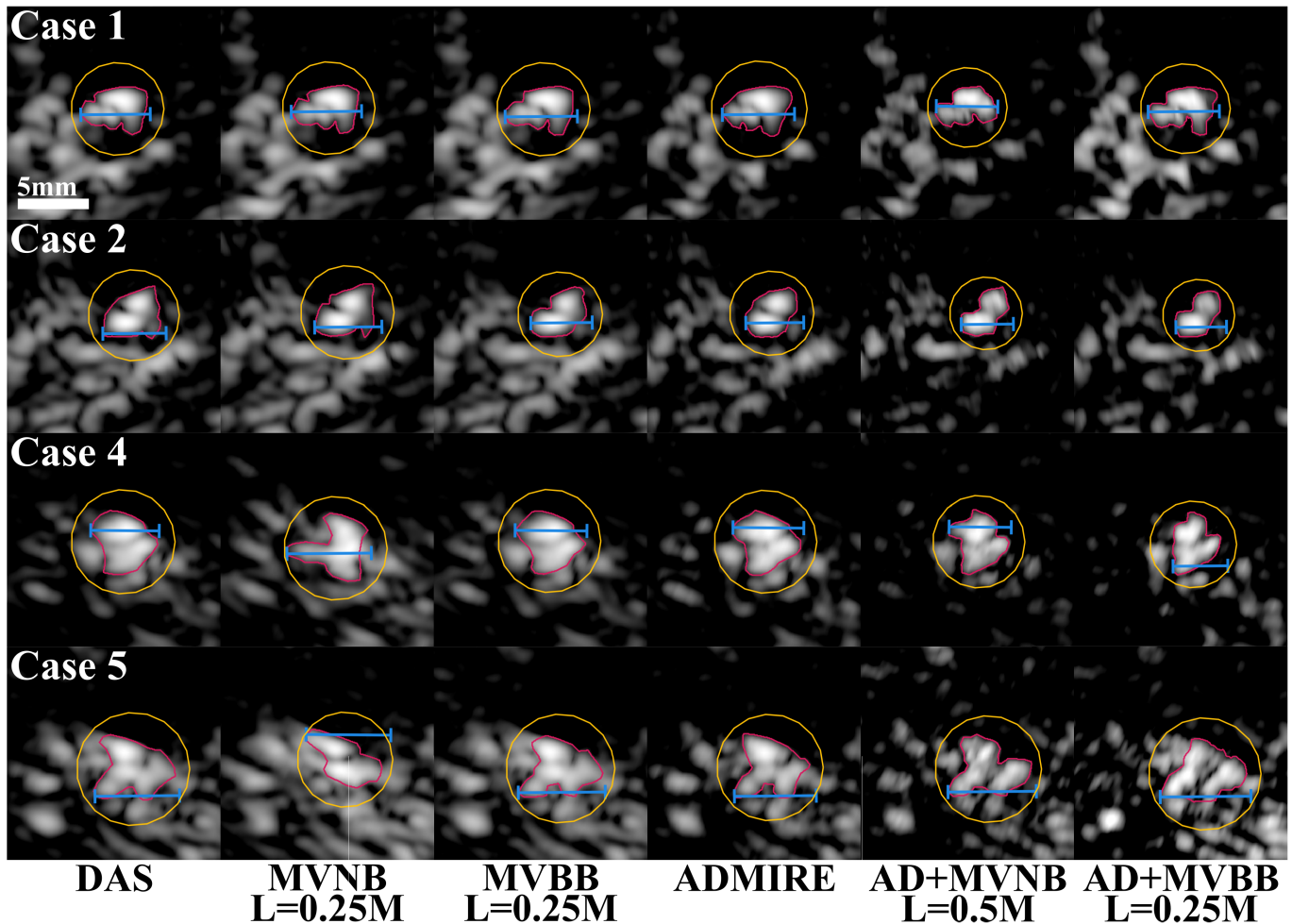
Fig. 7. B-mode images on a 30-dB dynamic range of a selection of the *in vivo* kidney stones. The individual stones are manually highlighted in red with the help of a contour map, and the background used for image quality metrics is shown in yellow based on the stone region selected. The blue line shows the lateral length of the stone region.

and considering the increased computation time the BB variant requires, it is easy to recommend MVNB as the more effective complement to ADMIRE.

ADMIRE as a choice for preprocessing performed as expected. From the cyst simulations for the specific interference sources, ADMIRE was visually able to suppress both types and improve image quality metrics compared to DAS. We additionally confirmed in simulated speckle phantoms that ADMIRE could produce significant improvements to SNR in the presence of thermal noise, and we similarly estimated SNR but for all noise types in the *in vivo* cases to demonstrate a similar level of improvement. Since MV performance is heavily dependent on the level of SNR of the image, this supports the idea that ADMIRE is a powerful option to improve MV in these low SNR cases. While we cannot specifically differentiate between reverberation clutter and other noise sources *in vivo* due to the lack of the additional frame data required, the simulations make it clear that reverberation clutter has a much stronger impact on MV performance compared to thermal noise.

Perhaps the main concern with implementing MV with ADMIRE, or MV in general, is the choice of parameters. We demonstrated that the subarray size by itself can have

a significant impact on resolution and general image quality, depending on what one is willing to sacrifice to boost the other. In simulations and simple imaging scenarios, it may be easy to sacrifice visibility to improve resolution, but, it is clear that, in more complex *in vivo* cases, this may not be true. Even as groups are investigating ways to automatically optimize these parameters, it is difficult to say how easy it will be to optimize these more complex cases. A consolation, perhaps, is that, regardless of what parameters we used in this work, AD + MVNB generated improvements compared to ADMIRE and MV, except in those *in vivo* cases where high subarray sizes degraded image quality so significantly that the image was no longer recognizable.

VII. Conclusion

We have shown in this work that, because ADMIRE and MV seek to improve images in different ways, this allows us to combine these methods to create images of superior quality than either method alone. In particular, we had hypothesized that MV would benefit from a denoising preprocessing step based on the fundamentals of the MV method, and we hoped that ADMIRE would benefit from improved lateral resolution. We implemented both NB and BB implementations of MV and

found that AD + MVNB produced *in vivo* images that were better than images from either method alone. AD + MVNB was able to improve resolution compared to just MVNB while simultaneously improving the contrast ratio that ADMIRE provides. Thus, not only did AD + MVNB attain the best image quality of both methods, it, in fact, managed to improve upon the best aspects of each as well. In future work, we will continue to investigate both how we can better tune ADMIRE and MV to further promote improved image quality, as well as investigate other methods that could be incorporated into the processing pipeline.

ACKNOWLEDGMENT

REFERENCES

[1] B. Byram, K. Dei, J. Tierney, and D. Dumont, "A model and regularization scheme for ultrasonic beamforming clutter reduction," *IEEE Trans. Ultrason., Ferroelectr., Freq. Control*, vol. 62, no. 11, pp. 1913–1927, Nov. 2015.

[2] K. Dei and B. C. Byram, "The impact of model-based clutter suppression on cluttered, aberrated wavefronts," *IEEE Trans. Ultrason., Ferroelectr., Freq. Control*, vol. 64, no. 10, pp. 1450–1464, Oct. 2017.

[3] B. Byram and M. Jakovljevic, "Ultrasonic multipath and beamforming clutter reduction: A chirp model approach," *IEEE Trans. Ultrason., Ferroelectr., Freq. Control*, vol. 61, no. 3, pp. 428–440, Mar. 2014.

[4] J. Capon, "High-resolution frequency-wavenumber spectrum analysis," *Proc. IEEE*, vol. 57, no. 8, pp. 1408–1418, Aug. 1969. [Online]. Available: http://ieeexplore.ieee.org/document/1449208/

[5] M. Sasso and C. Cohen-Bacrie, "Medical ultrasound imaging using the fully adaptive beamformer," in *Proc. IEEE Int. Conf. Acoust., Speech, Signal Process., (ICAASP)*, vol. 2, Mar. 2005, pp. 489–492. [Online]. Available: http://ieeexplore.ieee.org/document/1415448/

[6] J.-F. Synnevåg, A. Austeng, and S. Holm, "Adaptive beamforming applied to medical ultrasound imaging," *IEEE Trans. Ultrason., Ferroelectr., Freq. Control*, vol. 54, no. 8, pp. 1606–1613, Aug. 2007.

[7] I. K. Holfort, F. Gran, and J. A. Jensen, "Broadband minimum variance beamforming for ultrasound imaging," *IEEE Trans. Ultrason., Ferroelectr., Freq. Control*, vol. 56, no. 2, pp. 314–325, Feb. 2009.

[8] J.-F. Synnevåg, A. Austeng, and S. Holm, "Benefits of minimum-variance beamforming in medical ultrasound imaging," *IEEE Trans. Ultrason., Ferroelectr., Freq. Control*, vol. 56, no. 9, pp. 1868–1879, Sep. 2009.

[9] B. M. Asl and A. Mahloojifar, "Eigenspace-based minimum variance beamforming applied to medical ultrasound imaging," *IEEE Trans. Ultrason., Ferroelectr., Freq. Control*, vol. 57, no. 11, pp. 2381–2390, Nov. 2010.

[10] S. Mehdizadeh, A. Austeng, T. F. Johansen, and S. Holm, "Eigenspace based minimum variance beamforming applied to ultrasound imaging of acoustically hard tissues," *IEEE Trans. Med. Imag.*, vol. 31, no. 10, pp. 1912–1921, Oct. 2012.

[11] A. M. Deylami and B. M. Asl, "Iterative minimum variance beamformer with low complexity for medical ultrasound imaging," *Ultrasound Med. Biol.*, vol. 44, no. 8, pp. 1882–1890, 2018, doi: 10.1016/j.ultrasmedbio.2018.04.016.

[12] B. M. Asl and A. M. Deylami, "A low complexity minimum variance beamformer for ultrasound imaging using dominant mode rejection," *Ultrasonics*, vol. 85, pp. 49–60, Apr. 2018, doi: 10.1016/j.ultras.2017.12.012.

[13] K. Diamantis, T. Anderson, M. B. Butler, C. A. Villagomez-Hoyos, J. A. Jensen, and V. Sboros, "Resolving ultrasound contrast microbubbles using minimum variance beamforming," *IEEE Trans. Med. Imag.*, vol. 38, no. 1, pp. 194–204, Jan. 2019.

[14] W. Wang, S. Yan, L. Mao, and X. Guo, "Robust minimum variance beamforming with sidelobe-level control using the alternating direction method of multipliers," *IEEE Trans. Aerosp. Electron. Syst.*, vol. 57, no. 5, pp. 3506–3519, Oct. 2021.

[15] A. Salari and B. M. Asl, "User parameter-free minimum variance beamformer in medical ultrasound imaging," *IEEE Trans. Ultrason., Ferroelectr., Freq. Control*, vol. 68, no. 7, pp. 2397–2406, Jul. 2021.

[16] K. Dei, J. Tierney, and B. Byram, "Plane wave image quality improvement using ADMIRE algorithm," in *Proc. IEEE Int. Ultrason. Symp. (IUS)*, Sep. 2016, pp. 1–4.

[17] S. Schlunk and B. C. Byram, "Using ADMIRE to improve minimum variance performance in the presence of reverberation clutter," in *Medical Imaging: Ultrasonic Imaging and Tomography*, N. V. Ruiter and B. C. Byram, Eds. Bellingham, WA, USA: SPIE, 2021, [Online]. Available: https://www.spiedigitallibrary.org/conference-proceedings-of-spie/11602/2583314/Using-ADMIRE-to-improve-minimum-variance-performance-in-the-presence/10.1117/12.2583314.full

[18] H. L. Van Trees, "Optimum Waveform Estimation," in *Optimum Array Processing: Part IV of Detection, Estimation, and Modulation Theory*. New York, NY, USA: Wiley, Mar. 2002, ch. 6, pp. 428–709, doi: 10.1002/0471221104.

[19] F. Viola, M. A. Ellis, and W. F. Walker, "Time-Domain optimized near-field estimator for ultrasound imaging: Initial development and results," *IEEE Trans. Med. Imag.*, vol. 27, no. 1, pp. 99–110, Jan. 2008.

[20] M. V. Greening and J. E. Perkins, "Adaptive beamforming for nonstationary arrays," *J. Acoust. Soc. Amer.*, vol. 112, no. 6, pp. 2872–2881, Dec. 2002. [Online]. Available: http://ieeexplore.ieee.org/document/574504/, doi: 10.1121/1.1514931.

[21] H. Cox, "Adaptive beamforming in non-stationary environments," in *Proc. Conf. Rec. 36th Asilomar Conf. Signals, Syst. Comput.*, vol. 1, 2002, pp. 431–438. [Online]. Available: http://ieeexplore.ieee.org/document/1197220/

[22] P. Stoica, Z. Wang, and J. Li, "Robust capon beamforming," *IEEE Signal Process. Lett.*, vol. 10, no. 6, pp. 172–175, Jun. 2003. [Online]. Available: http://ieeexplore.ieee.org/document/1198667/

[23] H. Weyl, "Ausbreitung elektromagnetischer Wellen über einem ebenen Leiter," *Annalen Der Physik*, vol. 365, no. 21, pp. 481–500, Aug. 1919, doi: 10.1002/andp.19193652104.

[24] W. C. Chew, *Waves and Fields in Inhomogenous Media* (Series on Electromagnetic Wave Theory). Hoboken, NJ, USA: Wiley, 1995.

[25] N. Kinayman and M. I. Aksun, *Modern Microwave Circuits* (Artech House microwave library). Norwood, MA, USA: Artech House, 2005.

[26] J. A. Jensen, "FIELD: A program for simulating ultrasound systems," Paper presented at the 10th Nordic-Baltic Conf. Biomed. Imag. Published Med. Biol. Eng. Comput., vol. 34, 1996, pp. 351–353.

[27] J. A. Jensen and N. B. Svendsen, "Calculation of pressure fields from arbitrarily shaped, apodized, and excited ultrasound transducers," *IEEE Trans. Ultrason., Ferroelectr., Freq. Control*, vol. 39, no. 2, pp. 262–267, Jan. 1992.

[28] J. J. Dahl and N. M. Sheth, "Reverberation clutter from subcutaneous tissue layers: Simulation and *in Vivo* demonstrations," *Ultrasound Med. Biology*, vol. 40, no. 4, pp. 714–726, Apr. 2014. [Online]. Available: https://linkinghub.elsevier.com/retrieve/pii/S0301562913012271

[29] G. Pinton, G. E. Trahey, and J. J. Dahl, "Sources of image degradation in fundamental and harmonic ultrasound imaging using nonlinear, full-wave simulations," *IEEE Trans. Ultrason., Ferroelectr., Freq. Control*, vol. 58, no. 4, pp. 754–765, Apr. 2011.

[30] A. Austeng, T. Bjastad, J.-F. Synnevaag, S.-E. Masoy, H. Torp, and S. Holm, "Sensitivity of minimum variance beamforming to tissue aberrations," in *Proc. IEEE Ultrason. Symp.*, Nov. 2008, pp. 1072–1075.

[31] B. S. Robinson, A. Shmulewitz, and T. M. Burke, "Waveform aberrations in an animal model," in *Proc. IEEE Ultrason. Symp.*, vol. 3, Oct./Nov. 1994, pp. 1619–1624.

[32] J. J. Dahl et al., "Coherence beamforming and its applications to the difficult-to-image patient," in *Proc. IEEE Int. Ultrason. Symp. (IUS)*, Sep. 2017, pp. 1–10.

[33] G. Matrone, A. S. Savoia, G. Caliano, and G. Magenes, "The delay multiply and sum beamforming algorithm in ultrasound B-mode medical imaging," *IEEE Trans. Med. Imag.*, vol. 34, no. 4, pp. 940–949, Apr. 2015.

[34] H. Zou and T. Hastie, "Regularization and variable selection via the elastic net," *J. Roy. Statist. Soc., B, Stat. Methodol.*, vol. 67, no. 2, pp. 301–320, 2005.

[35] R. J. Tibshirani and J. Taylor, "Degrees of freedom in lasso problems," *Ann. Statist.*, vol. 40, no. 2, pp. 1198–1232, 2012.

[36] B. Yang, "A study of inverse short-time Fourier transform," in *Proc. IEEE Int. Conf. Acoust., Speech Signal Process.*, Apr. 2008, pp. 3541–3544.

[37] B. H. Friemel, L. N. Bohs, K. R. Nightingale, and G. E. Trahey, "Speckle decorrelation due to two-dimensional flow gradients," *IEEE Trans. Ultrason., Ferroelectr., Freq. Control*, vol. 45, no. 2, pp. 317–327, Mar. 1998.

[38] B. Byram and J. Shu, "Pseudononlinear ultrasound simulation approach for reverberation clutter," *Proc. SPIE*, vol. 3, no. 4, 2016, Art. no. 046005.

[39] B. Byram and J. Shu, "A pseudo non-linear method for fast simulations of ultrasonic reverberation," *Proc. SPIE*, vol. 9790, pp. 1–7, Apr. 2016.

[40] S. Schlunk, K. Dei, and B. Byram, "Iterative model-based beamforming for high dynamic range applications," *IEEE Trans. Ultrason., Ferroelectr., Freq. Control*, vol. 68, no. 3, pp. 482–493, Mar. 2020. [Online]. Available: https://ieeexplore.ieee.org/document/9149929/

[41] M. A. Lediju, M. J. Pihl, J. J. Dahl, and G. E. Trahey, "Quantitative assessment of the magnitude, impact and spatial extent of ultrasonic clutter," *Ultrason. Imag.*, vol. 30, no. 3, pp. 151–168, Jul. 2008.

[42] G. Montaldo, M. Tanter, J. Bercoff, N. Benech, and M. Fink, "Coherent plane-wave compounding for very high frame rate ultrasonography and transient elastography," *IEEE Trans. Ultrason., Ferroelectr., Freq. Control*, vol. 56, no. 3, pp. 489–506, Mar. 2009.

[43] A. Rodriguez-Molares, O. M. H. Rindal, J. D'Hooge, S.-E. Måsøy, A. Austeng, and H. Torp, "The generalized contrast-to-noise ratio," in *Proc. IEEE Int. Ultrason. Symp. (IUS)*, Oct. 2018, pp. 1–4.

[44] A. Rodriguez-Molares *et al.*, "The generalized contrast-to-noise ratio: A formal definition for lesion detectability," *IEEE Trans. Ultrason., Ferroelectr., Freq. Control*, vol. 67, no. 4, pp. 745–759, Apr. 2020. [Online]. Available: https://ieeexplore.ieee.org/document/8918059/

[45] N. Bottenus, M. LeFevre, J. Cleve, A. L. Crowley, and G. Trahey, "Resolution and speckle reduction in cardiac imaging," *IEEE Trans. Ultrason., Ferroelectr., Freq. Control*, vol. 3010, no. 4, pp. 1131–1143, Apr. 2020.

[46] E. Samei, M. J. Flynn, and D. A. Reimann, "A method for measuring the presampled MTF of digital radiographic systems using an edge test device," *Med. Phys.*, vol. 25, no. 1, pp. 102–113, 1998.

[47] J. Tierney *et al.*, "Non-linear beamforming approaches for sizing and detecting large calcifications," in *Proc. IEEE Int. Ultrason. Symp. (IUS)*, Sep. 2017, pp. 1–4. [Online]. Available: http://ieeexplore.ieee.org/document/8092597/

[48] R. S. Hsi *et al.*, "Feasibility of non-linear beamforming ultrasound methods to characterize and size kidney stones," *PLoS ONE*, vol. 13, no. 8, pp. 1–14, 2018.

[49] J. E. Tierney *et al.*, "*In vitro* feasibility of next generation non-linear beamforming ultrasound methods to characterize and size kidney stones," *Urolithiasis*, vol. 47, no. 2, pp. 181–188, 2019, doi: 10.1007/s00240-018-1036-z.

[50] E. P. Vienneau, K. A. Ozgun, and B. C. Byram, "Spatiotemporal coherence to quantify sources of image degradation in ultrasonic imaging," *IEEE Trans. Ultrason., Ferroelectr., Freq. Control*, vol. 69, no. 4, pp. 1337–1352, Apr. 2022.

[51] D. Hyun, A. L. C. Crowley, and J. J. Dahl, "Efficient strategies for estimating the spatial coherence of backscatter," *IEEE Trans. Ultrason., Ferroelectr., Freq. Control*, vol. 64, no. 3, pp. 500–513, Mar. 2017.

[52] W. Long, N. Bottenus, and G. E. Trahey, "Lag-one coherence as a metric for ultrasonic image quality," *IEEE Trans. Ultrason., Ferroelectr., Freq. Control*, vol. 65, no. 10, pp. 1768–1780, Oct. 2018.

[53] N. Bottenus, B. C. Byram, and D. Hyun, "Histogram matching for visual ultrasound image comparison," *IEEE Trans. Ultrason., Ferroelectr., Freq. Control*, vol. 3010, no. 5, pp. 1487–1495, May 2020.

Siegfried Schlunk (Student Member, IEEE) received the B.E. degree in biomedical engineering and mathematics from Vanderbilt University, Nashville, TN, USA, in 2016, where he is currently pursuing the Ph.D. degree in biomedical engineering.

His research interests focus on developing methods for improving ultrasound image quality in cardiac and kidney applications.

Brett Byram (Member, IEEE) received the B.S. degree in biomedical engineering and math from Vanderbilt University, Nashville, TN, USA, in 2004, and the Ph.D. degree in biomedical engineering from Duke University, Durham, NC, USA, in 2011.

He then stayed as a Research Assistant Professor at Duke University. In 2013, he joined the Biomedical Engineering Department, Vanderbilt University, as an Assistant Professor. He has spent time working at the Center for Fast Ultrasound, Jørgen Jensen, Lyngby, Denmark, and the Ultrasound Division, Siemens Healthcare, Mountain View, CA, USA. He currently runs the Biomedical Elasticity and Acoustic Measurement (BEAM) Laboratory, Vanderbilt University, where he and others in the lab pursue solutions to clinical problems using ultrasound. He is also with the Vanderbilt Institute for Surgery and Engineering (VISE) and the Vanderbilt University Institute of Imaging Science (VUIIS). His research interests include beamforming, motion estimation, and other related signal processing and hardware development tasks.